



DEPARTMENT OF THE NAVY

NAVAL SURFACE WARFARE CENTER

DAHLGREN, VIRGINIA 22448-5000

WHITE OAK
10901 NEW HAMPSHIRE AVE.
SILVER SPRING, MD. 20903-5000
(202) 394-

DAHLGREN, VA. 22448-5000
(703) 663-

IN REPLY REFER TO:

R42/5600
13 January 1992

Dr. Ronald C. Davidson, Editor
Physics of Fluids B: Plasma Physics
Princeton Plasma Physics Laboratory
James Forrestal Campus
P.O. Box 451
Princeton, NJ 08540

Dear Dr. Davidson:

Submitted herewith for inclusion in the Journal Physics of Fluids B: Plasma Physics is a paper entitled "Plasma Wakefield Effects on High-Current Relativistic Electron Beam Transport in the Ion-Focused Regime," by J. D. Miller, R. F. Schneider, D. J. Weidman, H. S. Uhm, and K. T. Nguyen of the Naval Surface Warfare Center.

This paper has been reviewed by cognizant naval authorities and is approved for public release. Further correspondence intended for the authors should be directed to the attention of Dr. Joel D. Miller, Naval Surface Warfare Center, Code R42, White Oak Laboratory, 10901 New Hampshire Avenue, Silver Spring, Maryland 20903-5000.

Sincerely,

CARL W. LARSON, HEAD
Physics and Technology Division

Encl: (1) 1 copy of publication

DISTRIBUTION STATEMENT A

Approved for public release;
Distribution Unlimited

DTIC QUALITY INSPECTED 4

PLEASE RETURN TO:

BMD TECHNICAL INFORMATION CENTER
BALLISTIC MISSILE DEFENSE ORGANIZATION
7100 DEFENSE PENTAGON
WASHINGTON D.C. 20301-7100

19980309 119

u5123

Accession Number: 5123

Publication Date: Jan 13, 1992

Title: Plasma Wakefield Effects On High-Current Relativistic Electron Beam Transport In The Ion-Focused Regime

Personal Author: Miller, J.D.; Schneider, R.F.; Weidman, D.J.; Uhm, H.S.; Nguyen, K.T.

Corporate Author Or Publisher: Naval Surface Warfare Center, White Oak Laboratory Silver Spring, MD
2

Comments on Document: From Poet; This is the copy of a paper that was submitted to the Journal Physics of Fluids B: Plasma Physics.

Descriptors, Keywords: Plasma Wakefield Accelerator PWFA Density Current Relativistic Electron Beam Transport Ionization Focused Regime IFR Oscillation Wave Laser Pulse Radius TMA Tube Physics Channel Energy

Pages: 42

Cataloged Date: Jul 05, 1994

Document Type: HC

Number of Copies In Library: 000001

Record ID: 28954

Source of Document: Poet

Plasma Wakefield Effects On High-Current
Relativistic Electron Beam Transport In The Ion-Focused Regime

J.D. Miller, R.F. Schneider, D.J. Weidman^(a), and H.S. Uhm
Naval Surface Warfare Center, Silver Spring, MD 20903-5000

and

K.T. Nguyen
Mission Research Corporation, Newington, VA 22122

Abstract

Modulation of the beam current has been observed during ion-focused regime (IFR) transport of a high-power relativistic electron beam propagating through a low-density background plasma. Injecting a high-current, high-energy electron beam into an IFR channel immersed in a background plasma induces plasma oscillations. These background plasma oscillations, induced by the risetime portion of the beam ejecting plasma electrons from the vicinity of the beam into the background plasma, give rise to a modulated axial electric field. This field travels with the beam leading to beam energy and current oscillations. In the experiment, a 1.7-MeV, 1-kA, risetime-sharpened electron beam is propagated on a KrF excimer laser-produced IFR channel in TMA gas, which is immersed in a low-density plasma-filled transport tube. We present experimental measurements and computer simulations demonstrating modulation of this high-current relativistic electron beam near the low-density background plasma frequency.

PACS numbers: 41.80.Ee, 52.40.Mj

I. INTRODUCTION

Plasma wakefields are well known in the high-energy physics community. The plasma wakefield accelerator (PWFA)¹ utilizes the longitudinal electric fields in plasma waves excited by a short duration bunched relativistic electron beam as a source of high accelerating gradients. In the PWFA, intense electron bunches are utilized as a driver beam to excite wakefields in a high-density plasma. These fields are then used to accelerate a low-current trailing beam.^{2,3} We report here experimental measurements on high-current (kA level) relativistic electron beams whose transport is strongly influenced by the self-induced wakefields.

A high-current relativistic electron beam injected into a preionized plasma channel causes channel electrons to be expelled by the electrostatic force generated by the head of the beam and permits stable electron beam transport.⁴⁻⁸ If the plasma channel is immersed in a low-density background plasma, as illustrated in Fig. 1, both channel electrons and plasma electrons out to the charge neutralization radius are ejected by the beam head, provided the combined channel and background plasma density is less than the beam density. The charge neutralization radius is the point at which the total enclosed channel and background plasma ion charge is equal to the beam charge. The charge neutralization radius can be easily shown to be

$$r_n = r_b \sqrt{\left[\left(\frac{r_c}{r_b} \right)^2 + \frac{(1 - (r_c / r_b)^2 f_e)}{g} \right]} \quad (1)$$

where r_b is the beam radius, r_c is the channel radius, $f_e = n_i / n_b$ is the space charge neutralization

fraction and is the ratio of the channel ion density to the electron beam density, and $g = n_p/n_b$ is the ratio of the plasma density outside the channel to the electron beam density. The background electrons beyond the charge neutralization radius are not expelled, but they are perturbed by the beam head and begin to oscillate at a frequency near that of the electron plasma frequency of the low-density background plasma, $\omega_p = (n_p e^2 / \epsilon_0 m_e)^{1/2}$. These radial plasma oscillations produce an electrostatic wakefield with electric field components in the radial and axial directions. The longitudinal component of this field, $E_z \cong E_o \sin(\omega_p t)$, traveling with the beam, causes accelerating and decelerating forces on beam electrons leading to beam energy and current modulation. These effects were first observed for high-current beams in computer simulations⁹ and were seen to lead to eventual beam disruption. Recently, direct experimental measurements have been made which confirm the existence of this phenomena.¹⁰

The intensity of the energy modulation and the resulting degree of current modulation through the beam pulse is determined by the strength of the wakefield. For an electron beam propagating through a uniform background plasma contained within a grounded conductor of radius r_w , the amplitude of the axial electric field has been determined, via computer simulation using the two-and-one-half dimensional PIC code MAGIC¹¹, to scale as

$$E_o = 0.18 n_p^{1/2} I_b \quad [V/cm], \quad (2)$$

where n_p is in units of cm^{-3} , and I_b is the beam current in kA. This scaling is valid for beam currents in the range $I_b \leq 2$ kA and beam rise times less than the background plasma period. This scaling indicates that the higher the plasma density, the stronger the beam modulation for the same propagation distance. Numerical simulations also indicate that the amplitude of the

plasma wakefield is reduced from that shown in Eq. (2) as the beam rise-time is increased. For long-range propagation, the initial beam rise-time is eroded away after some distance and the wakefield amplitude is again increased. For the present experimental configuration, the simulations have indicated that it will be necessary to sharpen the beam rise-time prior to injecting the beam into the wakefield chamber.

II. EXPERIMENTAL ARRANGEMENT

In the experiment, a 1.7-MeV, 6-kA, 30-ns electron beam produced by a Febetron 705 is passed through a beam risetime sharpener and matched onto a laser produced IFR channel in trimethylamine (TMA) gas. Figure 2 is a schematic diagram of the experiment. The electron beam is generated from a 2.5-cm-diam velvet cathode with a 2.2 cm anode-cathode gap. The electron beam is extracted into a beam risetime sharpening cell through a 6 μ m aluminized mylar anode foil. The risetime sharpener cell uses a single magnetic lens to preferentially focus the high energy portion of the beam at an aperture further downstream. This downstream aperture is a 3-cm-diam graphite aperture plate covered by a second aluminized mylar foil. The beam exiting the risetime sharpening cell is matched onto a KrF excimer laser ionized IFR channel in TMA. The TMA gas flowed through the transport chamber continuously to provide a stable gas pressure in the range 0.2 - 0.8 mTorr. These TMA pressures result in space-charge neutralization fractions sufficient to efficiently propagate the electron beam in the absence of a background plasma. The TMA gas pressure is low enough that beam-induced ionization from the REB is negligible. The beam risetime sharpener cell and the diode region are maintained at a lower

pressure, on the order of 10^{-5} Torr, to prevent diode shorting or gas focusing effects. The laser is fired to ionize the TMA typically 500 ns before the voltage was applied to the diode. The resulting laser produced channel is centered in a 0.5-m-diam, 3.6-m-long plasma filled transport chamber. The low-density background plasma filling the transport chamber is generated by a hot filament discharge in the low pressure TMA gas.

The beam current is monitored prior to injection into the plasma filled transport chamber and after exiting the chamber by resistive wall current monitors.¹² Uncalibrated, single-turn B-dot loops¹³ located axially along the transport chamber monitor the evolution of the modulation of the current. Diametrically opposing B-dot loops could also be configured to detect transverse beam centroid motion.¹³ It should be noted that both current monitors are sensitive to the net current flowing in the transport chamber. A scintillator-photodiode observed the x-ray signal emitted when the beam electrons were deflected to the wall at the end of the transport chamber to avoid striking the laser input window.

A. Beam Risetime Sharpening

The electron beam generated by the Febetron 705 nominally has a pulse shape that is roughly triangular both in voltage and current. The diode voltage is monitored with a capacitive voltage divider. The diode current is monitored with a Rogowski coil located immediately downstream of the anode foil. Typical beam voltage and diode current waveforms are shown in Fig. 3. The electron beam current risetime of 15-ns is several times the plasma oscillation period of the low-density background plasma filling the transport chamber. Ideally, a zero risetime

beam would result in maximum wakefield excitation.¹⁴ A zero risetime beam is difficult, if not impossible, to achieve in practice however. The risetime can be sharpened sufficiently to enhance the wakefield excitation to an observable level. This is desirable in the laboratory experiment due to the finite propagation distance available.

A simple method for shaping the output current pulse of a relativistic electron beam in vacuum has been implemented to sharpen the risetime of the Febetron generated beam.¹⁵ The technique utilizes a magnetic lens with a magnitude of about 1-kG to focus the beam. Passing beam electrons through the magnetic lens causes them to focus at different axial locations downstream from the lens depending upon their energy. The focal point of the beam current peak (corresponding to maximum energy) is then located furthest downstream. By placing a small aperture near the beam peak focal point, we let the portion of the beam near the peak pass through, while intercepting most of the early portion of the pulse which has spread out before it reaches the aperture. Similarly, the later portion of the pulse fall time will also be intercepted. This creates an electron beam with sharper rise and fall times resulting in a more uniform current profile. This technique results in a 1-kA electron beam exiting the risetime sharpening cell with a 5-ns risetime and a 13-ns flattop.

B. Laser Ionized Channels in TMA

The 3-cm-diam laser ionized channel was formed by two-step photoionization of TMA using a 750-mJ, 248-nm, 30-ns KrF excimer laser. Measurements were performed¹⁶ to characterize the laser photoionization of: (a) initially neutral TMA gas, and (b) TMA gas

partially ionized by a heated filament DC discharge operated in both a pulsed (ms timescale) and steady-state mode.

Well-defined ionization volumes have been demonstrated to be quite efficient using multiphoton ionization of organic molecules.^{17,18} In this experiment we use a high-power KrF excimer laser to ionize a channel in trimethylamine $[(\text{CH}_3)_3\text{N}]$ gas (TMA). Previous measurements¹⁹ have indicated that TMA has a high two-photon ionization cross-section at the KrF laser wavelength of 248 nm. In our application it is necessary to determine accurate parameters to allow the degree of ionization to be calculated for arbitrary laser properties. A simple model that agrees well with previous experimental data for fractional ionization yields on the order of 10^{-3} or less, is that the fractional ionization (the ratio of plasma density n_p to the neutral gas density n_o) depends quadratically on the laser fluence.²⁰ This relationship takes the form

$$\frac{n_p}{n_o} = CF^2 \quad (3)$$

where F is the laser fluence (mJ/cm^2) and C is the absolute ionization yield coefficient. Generally C is defined as $C = \alpha/h\nu\tau$, where α is the two-photon ionization coefficient, $h\nu$ is the photon energy, and τ is the laser pulse half-width. Previous measurements have determined the value for C to be in the range 1.52×10^{-6} to $1.83 \times 10^{-6} \text{ cm}^4/\text{mJ}^2$ for laser pulse widths between 13.2 and 5.65 ns respectively for KrF laser ionization of TMA.²⁰

The situation of particular interest to our experiment is whether this relationship is appropriate for laser photoionization of partially ionized TMA. The photoionization process may

be effected due to the presence of a low-density DC discharge. In addition, the presence of such a discharge may lead to fragmentation of the large organic molecules and a corresponding reduction in the photoionization efficiency.

The experimental setup used to measure the laser parameters was similar to that shown in Fig. 2. The beam size at the output window of the laser is approximately 1 cm x 2.7 cm. The measured beam divergence was found to be very close to the specified value of 0.2 mrad. The laser pulse width is monitored with a DC biased pin diode and has a FWHM of approximately 25 ns. The laser beam is passed through a prism to expand the cross-section to about 3.1 cm square, and then through two adjustable apertures in series to limit the beam cross-section in the test cell. The laser intensity was then assumed to be spatially uniform in the test region. The laser energy per pulse is measured using a Scientech calorimeter. The TMA pressure was measured with ionization gauges calibrated to a Baratron capacitance manometer. The test cell was initially evacuated to about 4×10^{-6} Torr and TMA was allowed to flow continuously through the chamber.

The degree of ionization produced in the chamber by the laser pulse is determined by collecting the charge obtained from a known laser volume on biased electrodes inserted into the test cell.¹⁶ The results of the ionization yield measurements performed in neutral TMA are shown in Fig. 4, which plots the fractional ionization as a function of the laser fluence. The measurements show the expected F^2 dependence over the range of the data. The absolute ionization yield coefficient is extracted by least squares fitting the experimental data to Eq. (3). This fit is shown as the solid line in Fig. 4. From this fit we have determined C to be 4.27×10^{-7}

cm^4/mJ^2 . This result is in reasonable agreement with the previous measurements²⁰ and supports the use of Eq. (3) to determine the plasma density for fractional ionization yields up to 10^{-3} .

The presence of the DC steady-state discharge influences this result considerably. The measurements made in the presence of the low-density discharge plasma utilized microwave resonator probe techniques²¹ and simple DC biased Langmuir probes²² collecting electron saturation current. The partially ionized plasma background was produced with a heated filament discharge operating in both a DC steady-state mode and a DC pulsed (ms timescale) mode and will be described in the next section. Figure 5 demonstrates the reduced photoionization yield of the TMA measured by the microwave resonator probe in the DC steady-state discharge. The fractional ionization is seen to be reduced by about a factor of two in the low-current discharges. The photoionization yield then seems to be less sensitive to further increases in discharge current. The solid lines are curves fitted to an exponential decay of the form $n=n_0e^{-I/I_0}$, characteristic of plasma loss due to diffusion. This effect is also observed with the DC biased Langmuir probe.

This result has been found to be due primarily to the fragmentation of the TMA molecules in the low-density steady-state plasma discharge. Measurements of the fragmentation of the TMA in the discharges was made with the quadrupole gas analyzer. A typical mass spectra of the constituents present in the neutral TMA gas is shown in Fig. 6(a). The TMA line (59 amu) is most prominent with the existence of a few impurities at much lower partial pressures. The presence of the DC steady-state discharge modifies the mass spectrum considerably as shown in Fig. 6(b). Most apparent is the reduction of the TMA line and the

increase in the impurity lines to about the same level. The increase in impurities is accounted for primarily by H, H₂, N, CH₃, and multiples of these. These are readily identifiable as fragments of TMA. Addition of argon (40 amu) as a buffer gas for the discharge did not aid in reducing the fragmentation as shown in Figs. 6(c) and (d).

The presence of the DC steady-state discharge resulted in an unacceptably large reduction in the photoionization yield of the TMA. For the relativistic electron beam transport experiments the plasma channel parameters must be independent of the low-density background plasma conditions. To reduce the fragmentation of the TMA, the low-density background plasma discharge was operated in a pulsed DC mode. In this case the high-voltage discharge was pulsed for times less than 1 ms. This resulted in significantly reducing the degree of TMA fragmentation as measured with the DC biased Langmuir probes¹⁶.

C. Large Volume Plasma Formation

To fill the relatively large transport chamber uniformly with low-density ($10^8 - 10^9 \text{ cm}^{-3}$) background plasma, we have utilized a technique based upon direct ionization of the background gas by low-energy electrons emitted from heated tungsten filaments.²³ Heated filament discharges are a very basic and well-established technique for plasma generation. An annular arrangement of the filaments produces a relatively uniform radial plasma density profile. Application of a weak axial confining magnetic field (on the order of 5 G) ensures axial plasma uniformity and provides plasma confinement. This field is sufficiently small so as not to influence the electron beam dynamics. The discharge is pulsed for durations on the order of 1-ms to reduce the level

of TMA fragmentation before the laser is fired.¹⁶ The Langmuir probe data indicates that the plasma is formed within the first 200 μ s and behaves as a steady-state for the remainder of the voltage pulse. Properties of the plasma are diagnosed using Langmuir probe techniques²² and a microwave resonator probe²¹ located at diagnostic ports as shown in Fig. 2.

Peak plasma densities as a function of the discharge current are shown in Fig. 7. The relationship between the plasma density and the discharge current is found to be approximately linear for these conditions. Note that the error bars on the Langmuir probe data in this and subsequent figures are indicative of relative errors only. The microwave resonator probe provides the more accurate absolute plasma density measurements. Electron temperature measurements made with the Langmuir probe ranged from 1 to 3 eV.

A combination of Langmuir probe geometries was used to provide axial, radial, and azimuthal probe adjustability. Data for the axial, radial, and azimuthal plasma density profiles were taken individually over several minutes while the discharge was operating in the DC steady-state mode using argon as the fill gas. The gross features of these plasma density profiles were later confirmed with the discharge operating in TMA. The radial and axial plasma density profiles under a variety of discharge conditions are shown in Figs 8(a) and 8(b) respectively. The radial plasma density profile is observed to be quite uniform inside the annular filament location before falling off close to the walls of the chamber. Similarly, the axial plasma density profile taken along half the length of the chamber shows good uniformity over 1.4 m before increasing somewhat near the end of the chamber where the filaments are located. Since the geometry of the chamber is symmetric on both ends, the midplane has been defined as the zero

point on this plot and measurements taken along one end only. The plasma density is adjustable in the range 10^8 to $5 \times 10^9 \text{ cm}^{-3}$.

III. EXPERIMENTAL RESULTS

Initial experimental measurements have demonstrated very well defined current oscillations impressed upon the electron beam after traversing the 3.6-m-long transport chamber. These oscillations are in the range 150 to 300 MHz and are very close to the electron plasma frequency of the low density background plasma. In the absence of the background plasma, the most efficient electron beam transport occurred for a space-charge neutralization fraction of $f_e \approx 0.9$ as determined by the laser channel ionization measurements. This is indicative of a fairly high transverse beam temperature and is common to electron beams generated and propagated using these techniques.²⁴

The evolution of the current oscillations is characterized in the typical waveforms shown in Fig. 9. Figure 9(a) shows the response of the resistive wall current monitors in the absence of the background plasma. The currents are shown prior to the entrance of the beam into the transport chamber (upper waveform) and after exiting the chamber (lower waveform). Examination of the transported current waveform indicates a steepening of the current risetime with an associated spike at the front end of the pulse. This is due to a combination of inductive beam erosion and the fact that the beam voltage pulse is nearly sinusoidal and varies throughout the current pulse.²⁵ Figures 2(b)-(d) illustrate the development of current oscillations with

increasing background plasma density. The plasma densities have been inferred from DC biased (+40 V) Langmuir probe data without any correction for finite sheath effects. The space charge neutralization fraction at the peak beam current for all the data presented here was $f_c \approx 0.9$, giving a neutralization radius, r_n , ranging from 3.0 cm (Fig. 9(b)) to 2.4 cm (Fig. 9(d)). For these experimental parameters, n_p/n_b assumes values in the range $0 \leq n_p/n_b \leq 0.06$, indicating that the low density background plasma does not contribute significantly to the space charge neutralization fraction of the channel. The data in Figs. 9(c) and (d) indicate that the current becomes severely modulated after only 3.6 m of transport in the plasma background. Measurements performed with the resistive wall current monitors and the B-dot loops configured to detect transverse beam motion observed no discernable indication of beam motion transverse to the direction of propagation. Increasing the plasma density higher than that shown in Fig. 9(d) resulted in loss of transport efficiency and eventual beam disruption as indicated by the current monitors and the x-ray signal picked up by the scintillator-photodiode. Although a useful indicator for gross beam dynamics, the response time of the scintillator was not fast enough to respond to the beam current modulation.

The frequency of oscillation is more readily determined from the unintegrated B-dot loop data. Figure 10 shows the unintegrated B-dot loop response from the probe located 0.9 m downstream from the entrance to the plasma-filled transport chamber. The current oscillations are quite clear and indicate an increasing frequency with increasing plasma density. The dependence of the background plasma density on the oscillation frequency obtained from the unintegrated B-dot loop data is shown in Fig. 11. The solid line represents a least squares fit of the data to a $n_p^{1/2}$ dependence. This functional dependence indicates that the experimentally

observed current oscillation frequency scales quite well with the low density background electron plasma frequency. Comparison of the experimentally observed oscillation frequencies with the electron plasma frequency of the low-density background plasma inferred from the DC biased Langmuir probe data, indicates that the experimentally observed oscillation frequency is between 75 to 80% that of the electron plasma frequency calculated from the Langmuir probe data. A quantitative comparison such as this however is difficult to state with a high degree of confidence due to the uncertainty in the plasma density inferred from the Langmuir Probe data (which may be as high as a factor of 2).

IV. COMPARISON WITH THEORY

A. Axisymmetric Plasma Wakefield Mode

In this section we theoretically investigate the current profile of the relativistic electron beam upon exiting the plasma filled transport chamber. We assume that the axial electric field of the wakefield has a sinusoidal waveform with axial wavenumber k . Due to inductive erosion at the beam head, the beam front velocity $\beta_f c$ is slightly less than the initial beam velocity $\beta_b c$. Labeling t_0 for the beam segment which enters the chamber at time $t=t_0$, we obtain the axial momentum change $\Delta p(z,t)^{26}$

$$\Delta p(z,t) = \frac{eE_0}{kc\Delta\beta} [\cos(\theta - k\Delta\beta ct_0) - \cos(\theta - k\Delta\beta ct)] \quad (4)$$

when the beam segment t_0 propagates to z at time t . Here the normalized velocity difference

$\Delta\beta = \beta_b - \beta_i$, E_0 is the maximum electric field of the wakefield given by Eq. (2), and the angle parameter θ is defined by $\theta = k\beta_b c t_0$. In our experiment, the combination of beam current and relatively short propagation distance make the inductive erosion rate rather small. In the absence of significant erosion, i.e., $\beta_b = \beta_i$, the momentum change in Eq. (4) is simplified to

$$\Delta p(z, t_0) = - \frac{eE_0 z}{\beta_b c} \sin\theta. \quad (5)$$

In reality, the velocity of the beam segment t_0 is continuously changing during the propagation and this velocity is expressed as $\beta c = p/\gamma m$, where the relativistic mass ratio γ is defined as $\gamma = (1 + p^2/m^2 c^2)^{-1/2}$, and the axial momentum p and the mass ratio γ are functions of the position z and time t . The velocity change $\delta\beta$ during the propagation is then related to the momentum change Δp by $\delta\beta = \Delta p/\gamma^3 m c$. The normalized axial velocity β of the beam segment t_0 is therefore expressed as $\beta = \beta_b + \delta\beta$, when it arrives at z . By approximating the mass ratio γ by γ_b , where γ_b is the initial beam energy, we can obtain the velocity from Eq. (5),

$$\frac{dz}{dt} = \beta c = \beta_b c \left[1 - \frac{1}{\gamma_b (\gamma_b^2 - 1)} \frac{eE_0 z}{mc^2} \sin\theta \right] \quad (6)$$

of the segment t_0 when it arrives at z . The approximation of γ by γ_b is valid only for $\gamma_b \gg 1$. Note that the velocity of the segment t_0 is $\beta c = \beta_b c$ at $z=0$ and that $\beta_b(t_0)$ is a function of t_0 in general. Thus, the average velocity of the segment t_0 over the range from $z=0$ to $z=z$ is given by

$$\langle \beta \rangle c = \beta_b c (1 - \kappa \sin\theta) \quad (7)$$

where the parameter κ is defined by

$$\kappa = \frac{1}{2\gamma_b(\gamma_b^2 - 1)} \frac{eE_0 z}{mc^2}. \quad (8)$$

In general, the parameter κ can be a function of t_0 .

Identifying the axial coordinate z by $z = \langle \beta \rangle c(t - t_0)$, we obtain the relationship between the time t and t_0 , which is

$$\phi = \theta + \frac{kz}{1 - \kappa \sin \theta}, \quad (9)$$

where the parameter ϕ is defined by $\phi = k\beta_b c t$ assuming that there is no beam head erosion. For simplicity it is assumed that β_b is constant throughout the beam pulse. Differentiating ϕ with respect to θ and defining $\chi = \kappa k z$, we find

$$\frac{d\phi}{d\theta} = 1 + \chi \frac{\cos \theta}{(1 - \kappa \sin \theta)^2}. \quad (10)$$

For a relatively moderate wakefield strength characterized by $\kappa \ll 1$, Eq. (10) can be simplified to

$$\frac{d\phi}{d\theta} = 1 + \chi \cos \theta \quad (11)$$

The condition $\kappa \ll 1$ can easily be satisfied by a broad range of physical parameters.

Note that the initial beam current $I_b(t_0)$ enters continuously through the chamber entrance located at $z=0$ and time $t=t_0$. When this beam segment arrives at $z=z$ in time t , this beam segment is stretched by the factor dt/dt_0 . Therefore, the beam current of the segment t_0 at z is

proportional to $d\theta/d\phi$. Making use of the normalization factor

$$\frac{1}{\pi} \int_0^\pi \frac{dx}{1 + a \cos x} = \frac{1}{\sqrt{1 - a^2}}, \quad (12)$$

we obtain the beam current $I(t_0)$

$$\frac{I(t_0)}{I_b(t_0)} = \frac{\sqrt{1 - \chi^2}}{1 + \kappa \cos \theta}, \quad (13)$$

assuming that there is no beam loss during the propagation. In reality however, we can expect beam current loss and approximate this with a fractional propagation factor α , which is in the range $0 < \alpha < 1$. In obtaining Eq. (13), we have assumed that the parameter κ is less than unity, which is valid for a limited propagation distance.

We have made several assumptions in the preceding analysis. First, beam-head erosion is negligibly small. For the beam parameters in the experiment, this is a reasonable approximation due to transient effects resulting from the relatively short propagation length. Second, although beam segments can be stacked up to each other, individual beam segments do not cross. Third, the beam segment gains or loses energy according to a predetermined sinusoidal waveform. In reality, the energy-gain mechanism of a beam segment may be much more complicated than a simple sinusoidal wave pattern. This simple theoretical description does however provide a basic understanding of the beam current profile at the end of the chamber.

For comparison, we consider the case for the background plasma density $n_p = 10^9 \text{ cm}^{-3}$, which corresponds to the plasma frequency $\omega_p = 1.78 \times 10^9 \text{ rad/s}$. The wakefield frequency is

expressed as^{14,26} $\omega = \sqrt{q} \omega_p$, where the crossover parameter q is typically 0.65. Thus, the wakefield frequency is $\omega = 1.43 \times 10^9$ rad/s. We also assume that the beam energy is about 1.1-MeV, which represents an average value of the beam energy throughout the beam pulse. The relativistic mass ratio is $\gamma_b = 3.2$. The beam current at the injection point is 500 A and the space-charge neutralization fraction is $f_e = 0.5$. The beam risetime is assumed to be $t_r = 5$ ns. These conditions are a good approximation to the experimental realization described previously. The maximum electric field E_0 of the wakefield wave is not sensitively dependent upon the beam radius for beam risetimes longer than one plasma oscillation period.¹⁴ Making use of these conditions, we find $E_0 = 2.8$ kV/cm from Eq. (2). Estimating the chamber length to be about 3.5 m, we find that $\kappa = 3 \times 10^{-2}$. Note that the value of the parameter κ is very small. The parameter χ is given by $\chi = 0.53$.

Shown in Fig. 12 are plots of the input and output current ratio $I(\theta)/I_b(\theta)$ versus θ obtained from Eq. (13) for $\chi = 0.53$, and $\alpha = 1$ and $\alpha = 0.5$. Here $\alpha = 1$ represents the case of no beam electron loss and $\alpha = 0.5$ means that one-half of the beam electrons are lost during propagation. As expected, the output beam current has very sharp peaks at $\theta = (2n+1)\pi$, where $n = 0, 1, 2, \dots$ is an integer. Note that this simple theoretical estimation of the output current profile is very similar to the experimentally observed data.

It is interesting to note that for long distance propagation, in the case where the parameter χ is larger than unity, the solution indicates that the current $I(t_0)$ has two cusped peaks for each period of the wakefield oscillation. Symptoms of this behavior have been observed in

the particle simulation studies²⁶ of long distance beam propagation and also appear to be evident in the present experiment and simulations.

B. Numerical Simulations

Numerical simulations have been performed to predict the behavior of the electron beam in the plasma filled chamber using the fully electromagnetic 2-1/2 dimensional particle-in-cell code MAGIC.¹¹ This code was developed for simulating axisymmetric plasma phenomena such as the case at hand. The beam and channel properties in the simulation correspond quite closely to the experimental conditions described previously. The simulation parameters are listed in Table 1. The beam initial energy had an isosceles triangle profile with a base of 640 kV and a peak of 1.7 MV. The transport chamber was filled with a uniform diffuse plasma with a density that could be varied, although unless otherwise indicated, the simulation results shown here will be at a background plasma density of $2 \times 10^9 \text{ cm}^{-3}$.

Shown in Fig. 13 is an electron trajectory plot consisting of both beam electrons and background plasma electrons. The electron beam is propagating from left to right in each frame. In frame (a), the trajectory of the electrons are shown 4.8 ns after injection into the plasma chamber. As expected, the beam head is expanding radially since there is no electrostatic focusing force. Further back from the beam head, as the channel and background plasma electrons are ejected from the vicinity of the beam the beam is able to propagate in a focused manner. Figure 13(b) shows the evolution of this behavior at 9.6 ns. In this frame, oscillations of the background plasma about the charge neutralization radius are clearly apparent. By 28.8

ns into the pulse (Fig. 13(d)), the beam is actually being chopped up into beamlets.

The ability of the diffuse plasma wakefields to strongly modulate the beam energy is clearly shown in the beam axial momentum plot in Figure 14(a). The wakefield is the result of the diffuse plasma oscillations seen in Fig. 13(a)-(d). The axial length of the wakefield shown in Fig. 14 corresponds very favorably with the plasma wavelength of 75 cm expected for a diffuse background plasma density of $2 \times 10^9 \text{ cm}^{-3}$. This can also be observed in the axial electric field plot at the corresponding time ($t=19 \text{ ns}$) as shown in Fig. 14(b). One particular feature which can be noted from Fig. 14(b) is the growing amplitude of the wakefield as a function of axial distance. We believe this is due to the fact that as the beam energy is modulated by the wakefield, the beam bunches as it propagates downstream. The modulated beam current resonantly pumps the diffuse plasma, enhancing the wakefield amplitude, which in turn accelerates the beam bunching process.

The axial evolution of this bunching process on the electron beam current in the transport chamber is shown in Fig. 15(a)-(d). By the time the electron beam reaches the end of the 3.6 m transport chamber, the beam current is quite strongly bunched. This result compares very well with the experimental data shown in Fig. 9(d). The number of peaks (bunches) observed in the simulation of Fig. 15(d) is in excellent agreement with the experimental observations. It is interesting to note that the bunching frequency observed in the simulation is about 320 MHz, or 20% below the expected plasma frequency of 400 MHz for $n_p = 2.0 \times 10^9 \text{ cm}^{-3}$. Also notable in the frames of Fig. 15 is the generation of modulated plasma currents after the end of the beam current pulse. This effect is also quite apparent in the experimental data of Fig. 9. It is

worthwhile to point out that the relatively larger peaks of the current in the simulations are due to the fact that the current is integrated over the whole cross-section of the wakefield chamber. In the experiments, the current was measured with a resistive wall current monitor located at the edge of a smaller (15 cm diameter) transport tube a short distance downstream of the wakefield chamber.

A more direct comparison between the simulation results and the experimental data is shown in Fig. 16. The beam current profiles in Fig. 16(a)-(d) correspond closely to the experimental conditions shown in Fig. 9(a)-(d). The simulation clearly shows the ability of the diffuse plasma to strongly modulate the beam current. The simulation result compares very well to the experimental data. Figure 16(a) even shows the current spike at the front of the beam due to the combination of inductive erosion and the triangular beam voltage profile.

V. SUMMARY

We have observed very well-defined current oscillations impressed upon a high-current relativistic electron beam propagating in an IFR channel immersed in a low-density background plasma. Severe effects on beam current transport have been observed for g parameter values in the range 0.03 to 0.06 after only 3.6 m of beam transport. Initial results indicate the frequency of current oscillation to be near the plasma frequency of the low-density background plasma, consistent with the predictions of plasma wakefield theory. Numerical simulations using the 2-1/2 dimensional particle-in-cell code MAGIC are in very good agreement with the experimental

measurements.

ACKNOWLEDGMENTS

The authors would like to thank J. Goldhar, K. Struve, and W.C. Freeman for technical assistance, and G. Joyce for helpful discussions. Thanks also to R.A. Stark for performing some of the MAGIC simulations. This work was supported by the Strategic Defense Initiative Organization under funding document number N0001490WX15505 and Independent Research funds at the Naval Surface Warfare Center.

^(a) permanent address: Advanced Technology and Research, Laurel, MD 20707

¹ P. Chen, J.M. Dawson, R.W. Huff, and T. Katsouleas, Phys. Rev. Lett. **54**, 693 (1985).

² J.B. Rosenzweig, P. Schoessow, B. Cole, W. Gai, R. Konecny, J. Norem, and J. Simpson, Phys. Rev. A **39**, 1586 (1989).

³ J.B. Rosenzweig, D.B. Cline, B. Cole, H. Figueroa, W. Gai, R. Konecny, J. Norem, P. Schoessow, and J. Simpson, Phys. Rev. Lett. **61**, 98 (1988).

⁴ W.E. Martin, G.J. Caporaso, W.M. Fawley, D. Prosnitz, and A.G. Cole, Phys. Rev. Lett. **54**, 685 (1985); G.J. Caporaso, F. Rainer, W.E. Martin, D.S. Prono, and A.G. Cole, Phys. Rev. Lett. **57**, 1591 (1986).

⁵ R.L. Carlson, S.W. Downey, and D.C. Moir, J. Appl. Phys. **61**, 12 (1986).

⁶ C.A. Frost, S.L. Shope, R.B. Miller, G.T. Leifeste, C.E. Crist, and W.W. Reinstra, IEEE Trans. Nucl. Sci. NS-32, 2754 (1985).

⁷ H.L. Buchanan, Phys. Fluids **30**, 231 (1987).

⁸ S.L. Shope, C.A. Frost, G.T. Leifeste, and J.W. Poukey, Phys. Rev. Lett. **58**, 531 (1987).

⁹ M.A. Mostrom and B.S. Newberger, Bull. Am. Phys. Soc. **31**, 1399 (1986).

¹⁰ J.D. Miller, R.F. Schneider, D.J. Weidman, H.S. Uhm, and K.T. Nguyen, Phys. Rev. Lett. **67**, 1747 (1991).

¹¹ B. Goplen, L. Ludeking, J. McDonald, G. Warren, and R. Worl, Mission Research Corporation Report No. MRC/WDC-R-216, 1989, unpublished.

¹² K.W. Struve, Conference Record of the Workshop on Measurements of Electrical Quantities in Pulse Power Systems II, (IEEE Catalog No. 86CH2327-5, 1988), p. 36.

¹³ S. Humphries, Jr., Principles of Charged Particle Acceleration, (Wiley, New York, 1986), p. 278.

- ¹⁴ H.S. Uhm, Phys. Lett. A **149**, 469 (1990).
- ¹⁵ J.D. Miller, K.T. Nguyen, R.F. Schneider, K.W. Struve, and D.J. Weidman, Rev. Sci. Instrum. **62**, 2910 (1991).
- ¹⁶ J.D. Miller, R.F. Schneider, and J. Goldhar, Naval Surface Warfare Center Technical Note, NAVSWC TN 90-326, 1990, unpublished.
- ¹⁷ C. A. Frost, J.R. Woodworth, J.N. Olsen, and T.A. Green, Appl. Phys. Lett. **41**, 813 (1982).
- ¹⁸ J.R. Woodworth, T.A. Green, and C.A. Frost, J. Appl. Phys. **57**, 1648 (1985).
- ¹⁹ Long C. Lee, and William K. Bischel, J. Appl. Phys. **53**, 203 (1982).
- ²⁰ William K. Bischel, Leonard J. Jusinski, Mark N. Spencer, and Donald J. Eckstrom, J. Opt. Soc. Am. B **2**, 877 (1985).
- ²¹ R.L. Stenzel, Rev. Sci. Instrum. **47**, 603 (1976).
- ²² F.F. Chen, in Plasma Diagnostics Techniques, R.H. Huddleston and S.L. Leonard, eds., (Academic Press, New York, 1965), p. 113.
- ²³ J.D. Miller, R.F. Schneider, H.S. Uhm, and D.J. Weidman, Naval Surface Warfare Center Technical Note, NAVSWC TN 90-428, 1990, unpublished; H.S. Uhm, J.D. Miller, R.F. Schneider, and D.J. Weidman, IEEE Trans. Plasma Sci. **PS-19**, 535 (1991).
- ²⁴ J.D. Miller and R.M. Gilgenbach, IEEE Trans. Plasma Sci. **PS-18**, 658 (1990).
- ²⁵ J.R. Smith (private communication).
- ²⁶ H.S. Uhm and G. Joyce, Phys. Fluids B **3**, 1587 (1991).

TABLE CAPTION

Table 1. MAGIC simulation parameters.

FIGURE CAPTIONS

- Figure 1. Pictorial representation of an electron beam propagating on an IFR channel immersed in a low-density background plasma.
- Figure 2. Schematic of the plasma wakefield experiment.
- Figure 3. Diode voltage and current waveforms.
- Figure 4. Measurement of photoionization yield for TMA: \circ parallel plate ionization detector, \square microwave resonator probe.
- Figure 5. Photoionization yield for TMA in a steady-state, low-density dc discharge plasma. Laser fluence is 38.1 mJ/cm^2 for the hollow symbols, and 36.9 mJ/cm^2 for the solid symbols: \circ no background plasma, ∇ $n_p = 2.3 \times 10^8 \text{ cm}^{-3}$, \square $n_p = 5.6 \times 10^8 \text{ cm}^{-3}$, \bullet no background plasma, \blacktriangledown $n_p = 2.3 \times 10^8 \text{ cm}^{-3}$.
- Figure 6. Mass spectra of a steady-state dc discharge in TMA: (a) no plasma discharge, TMA pressure $6.8 \times 10^{-5} \text{ Torr}$, (b) 1.0 A plasma discharge current, $6.8 \times 10^{-5} \text{ Torr}$, (c) no plasma discharge, TMA pressure $6.8 \times 10^{-5} \text{ Torr}$ with $1.1 \times 10^{-4} \text{ Torr Ar}$, (d) 1.0 A plasma discharge, TMA pressure $6.8 \times 10^{-5} \text{ Torr}$ with $1.1 \times 10^{-4} \text{ Torr Ar}$.
- Figure 7. Plasma density as a function of discharge current. Discharge voltage = -70 V,

confining magnetic field = 5 G. Hollow symbols are argon at 5×10^{-4} Torr, filled symbols are TMA at 6.6×10^{-4} Torr. Circles represent Langmuir probe data, squares represent microwave resonator probe data.

Figure 8. Normalized (a) radial plasma density profiles in argon: discharge voltage is -70 V; \circ 2.0 A discharge current, 5 G magnetic field, 2×10^{-4} Torr, $z=0$ m, normalized to $4.4 \times 10^8 \text{ cm}^{-3}$, \square 1.25 A discharge current, 7.5 G magnetic field, 2×10^{-4} Torr, $z=0$ m, normalized to $5.0 \times 10^8 \text{ cm}^{-3}$, Δ 2.0 A discharge current, 5 G magnetic field, 2×10^{-4} Torr, $z=1.1$ m, normalized to $5.3 \times 10^8 \text{ cm}^{-3}$, and (b) on axis axial plasma density profiles in argon: discharge voltage = -70 V, magnetic field = 5 G, \circ 2.0 A discharge current, 2×10^{-4} Torr, normalized to $4.0 \times 10^8 \text{ cm}^{-3}$, \square 3.0 A discharge current, 5×10^{-4} Torr, normalized to $6.0 \times 10^8 \text{ cm}^{-3}$.

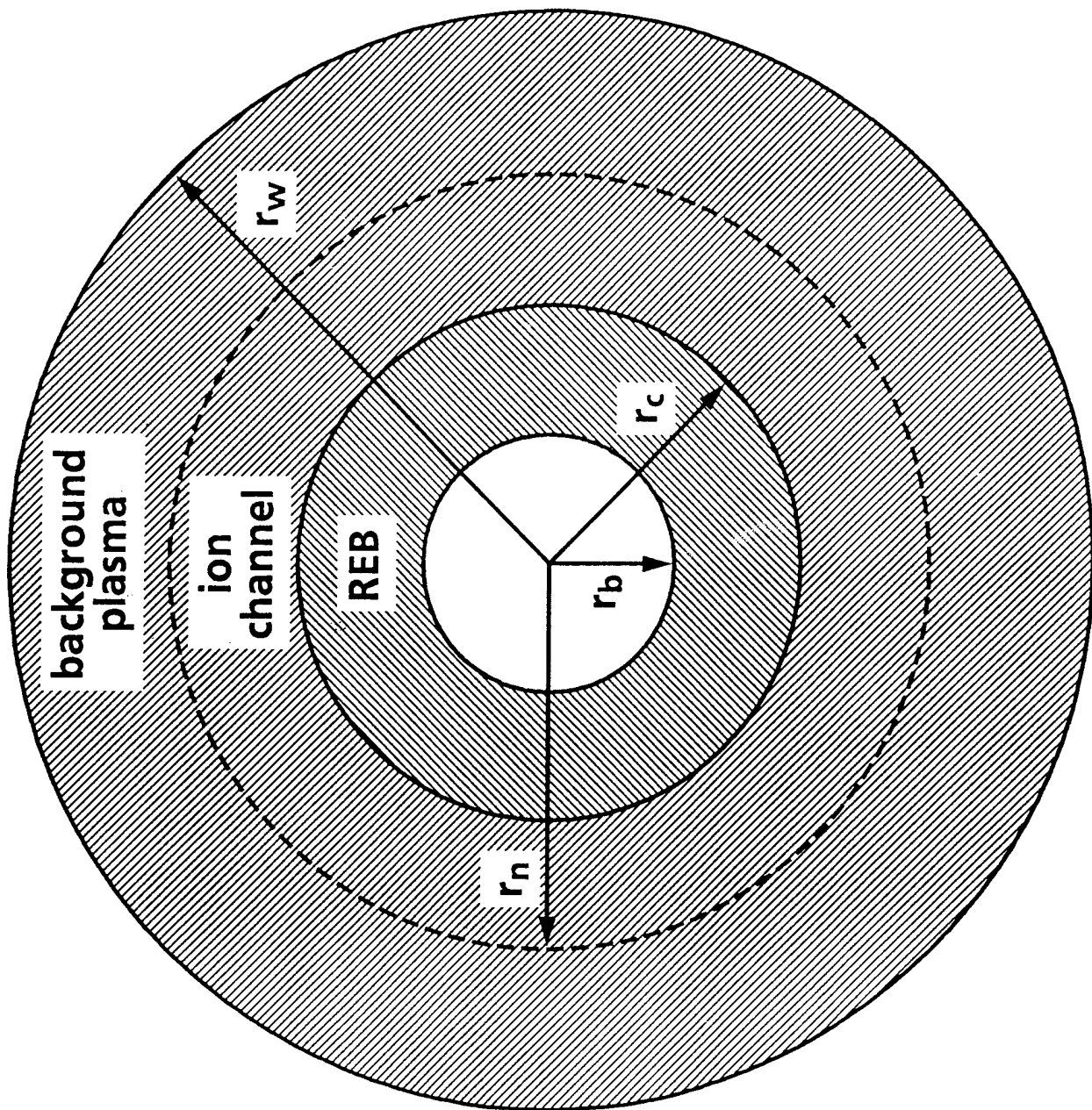
Figure 9. Current waveforms from the resistive wall current monitors; (a) $n_p=0$, (b) $n_p=1.0 \times 10^9 \text{ cm}^{-3}$, (c) $n_p=1.5 \times 10^9 \text{ cm}^{-3}$, (d) $n_p=2.0 \times 10^9 \text{ cm}^{-3}$. Top (bottom) waveform: current entering (exiting) the transport chamber.

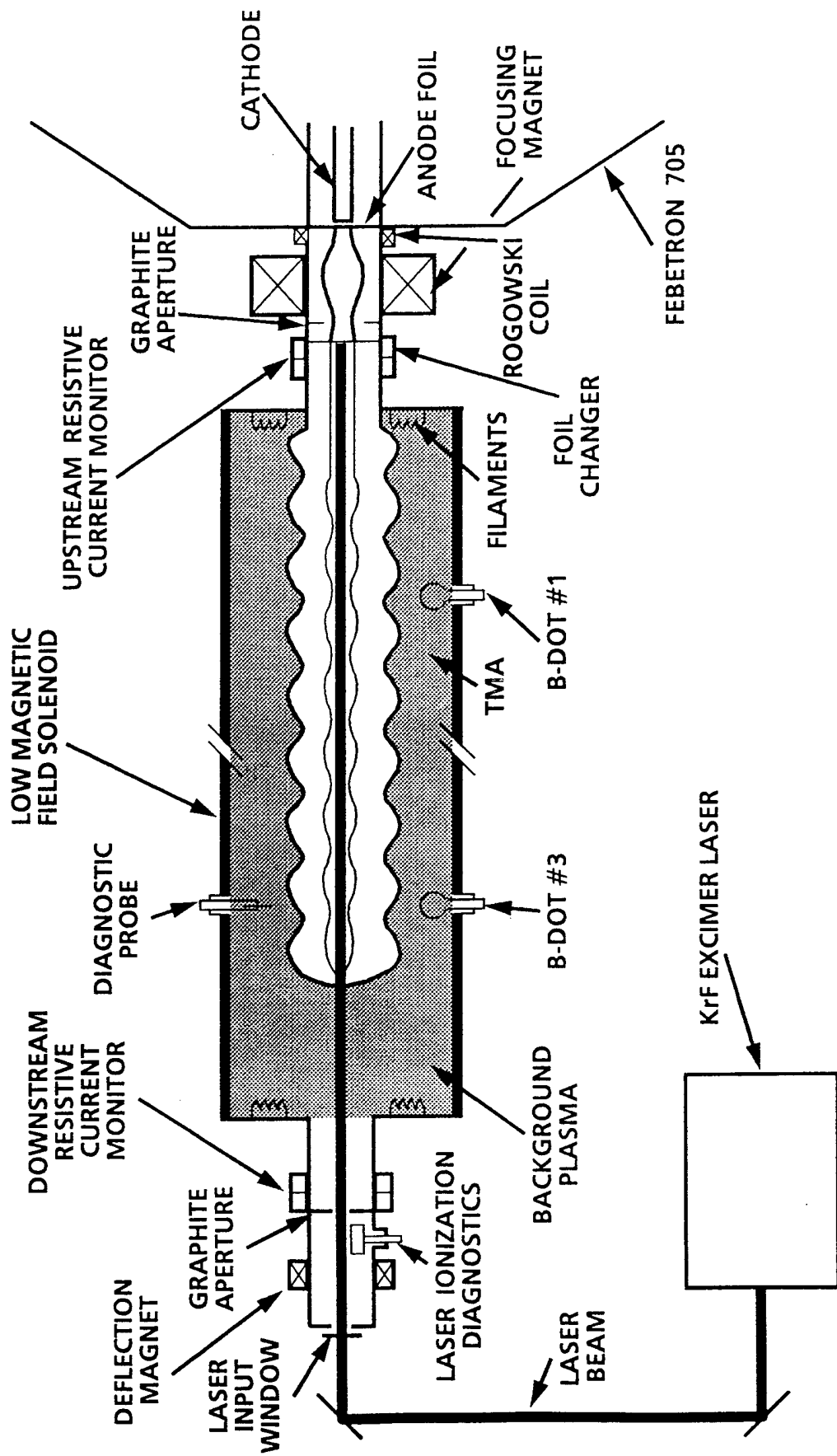
Figure 10. Unintegrated B-dot loop response 0.9 m downstream from the entrance to the plasma filled transport chamber; (a) $n_p=0$, (b) $n_p=6.3 \times 10^8 \text{ cm}^{-3}$, (c) $n_p=1.0 \times 10^9 \text{ cm}^{-3}$, (d) $n_p=1.5 \times 10^9 \text{ cm}^{-3}$.

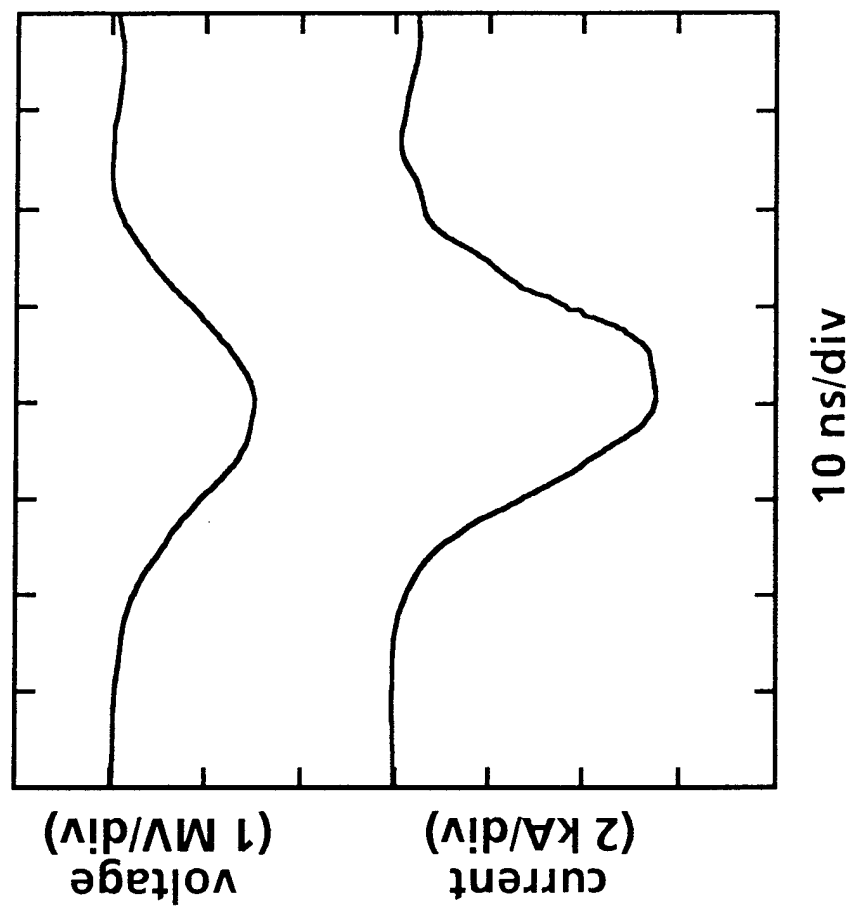
Figure 11. Oscillation frequency from the unintegrated B-dot loop data as a function of the background plasma density. The solid line is a least squares fit to $n_p^{1/2}$.

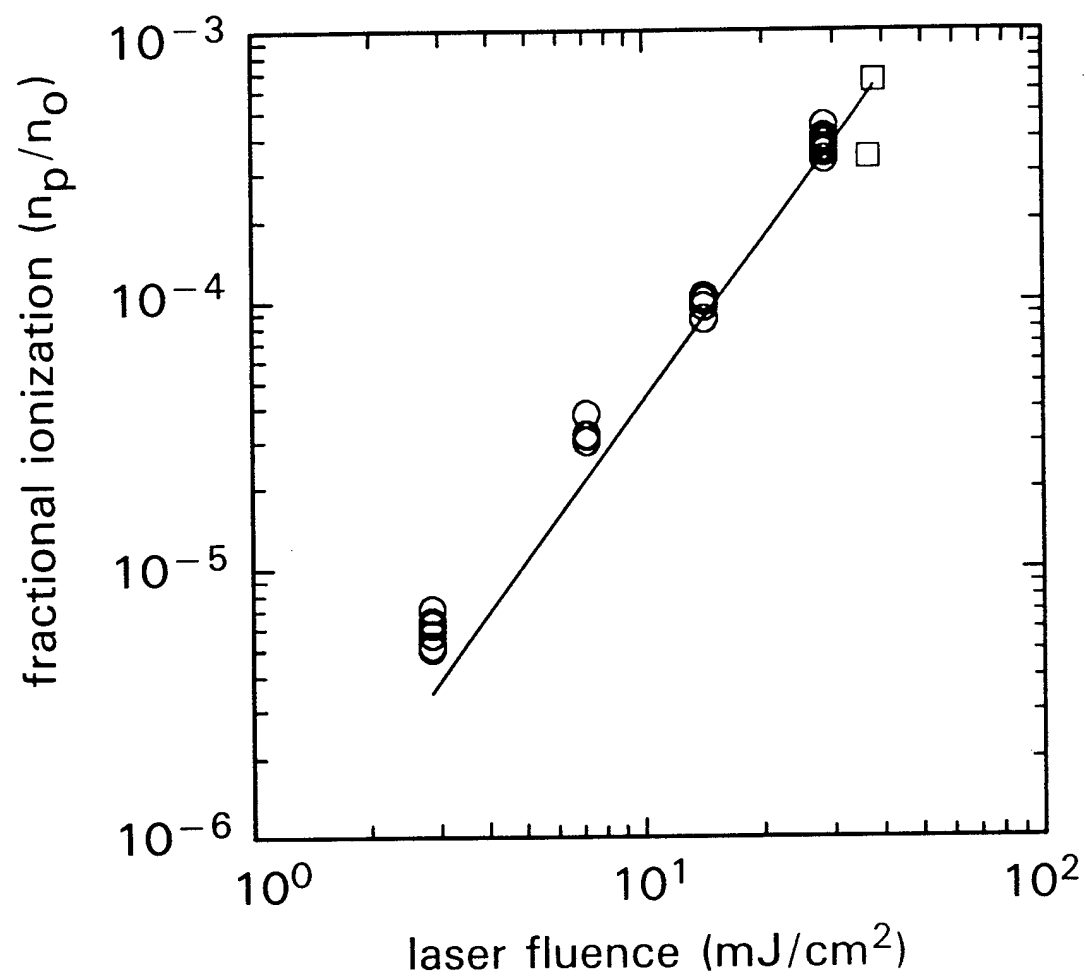
- Figure 12. Plots of the output to input beam current ratio versus θ obtained from Eq. (13).
- Figure 13. Plasma and beam electron trajectories from the MAGIC simulation for parameters as listed in Table 1.
- Figure 14. Electron beam axial momentum (a) and the axial electric field (b) at $t=19$ ns from injection into the plasma chamber.
- Figure 15. Beam current waveforms from the MAGIC simulation at (a) $z=0$ m, (b) $z=1.2$ m, (c) $z=2.4$ m, and (d) $z=3.6$ m downstream from the entrance to the plasma filled transport chamber for $n_p=2.0 \times 10^9 \text{ cm}^{-3}$.
- Figure 16. Beam current waveforms from the MAGIC simulation for (a) no background plasma, (b) $n_p=1.0 \times 10^9 \text{ cm}^{-3}$, (c) $n_p=1.5 \times 10^9 \text{ cm}^{-3}$, and (d) $n_p=2.0 \times 10^9 \text{ cm}^{-3}$, 3.6 m downstream from the entrance to the plasma filled transport chamber.

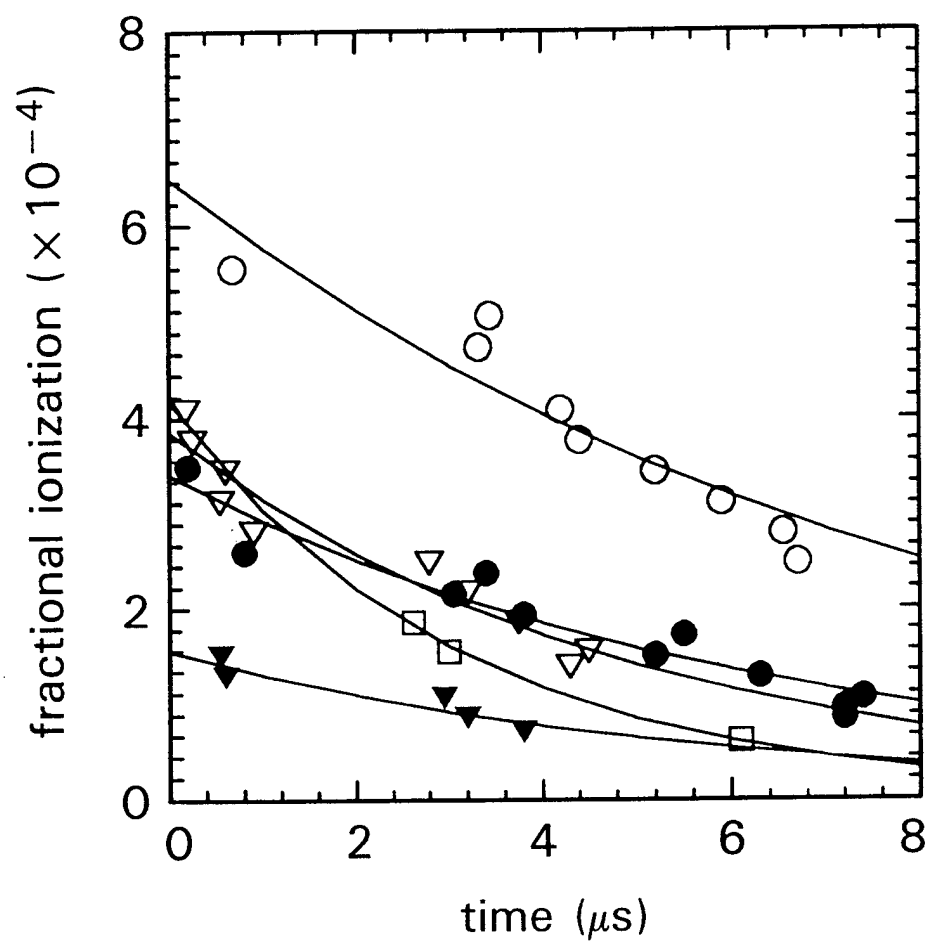
SYMBOL	PARAMETER	VALUE
I_b	beam current	1.0 kA
r_{bo}	initial beam radius	1.5 cm
V	beam voltage	1.7 MV
τ_r	beam risetime	5 ns
γ	relativistic mass factor	4.5
kT_{\perp}	initial transverse temperature	1.65γ keV
f_e	channel neutralization factor	0.8
r_c	channel radius	1.5 cm
n_p	background plasma density	$0-2 \times 10^9$ cm ⁻³
r_w	wakefield chamber radius	25 cm
L_w	wakefield chamber length	3.6 m

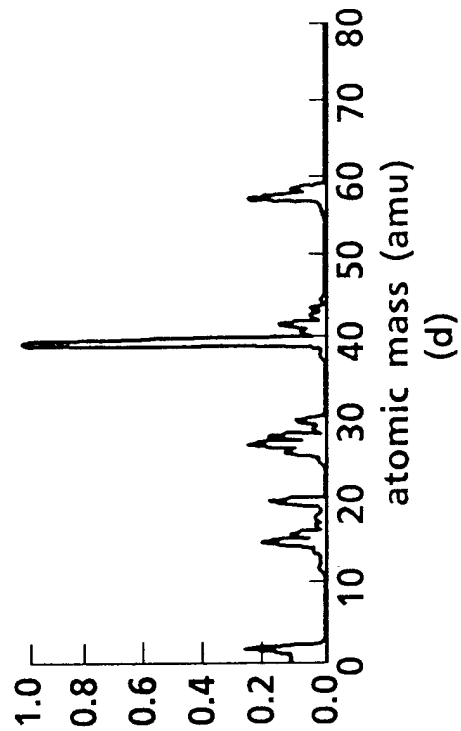
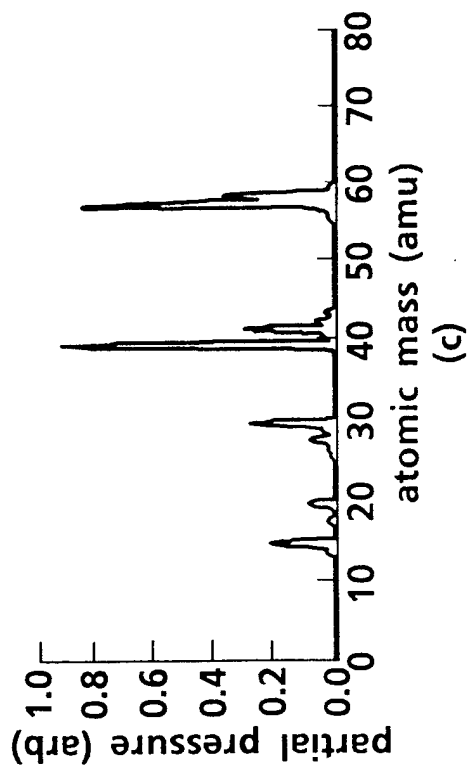
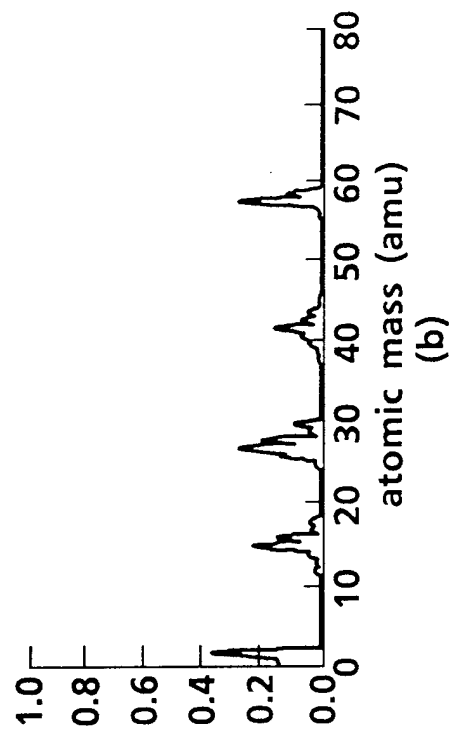
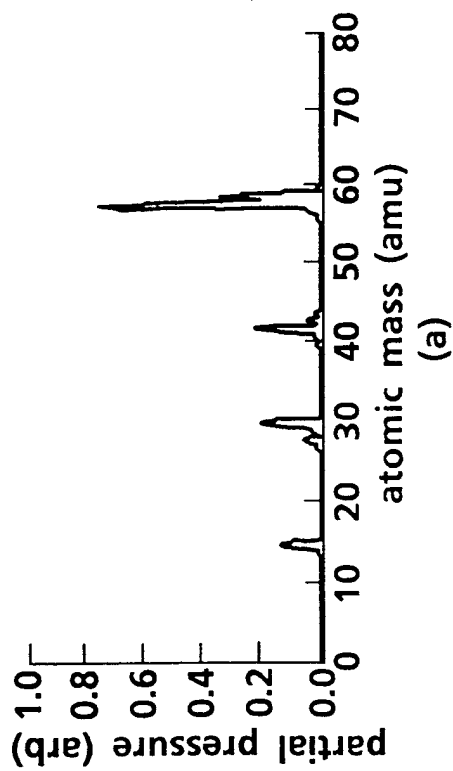


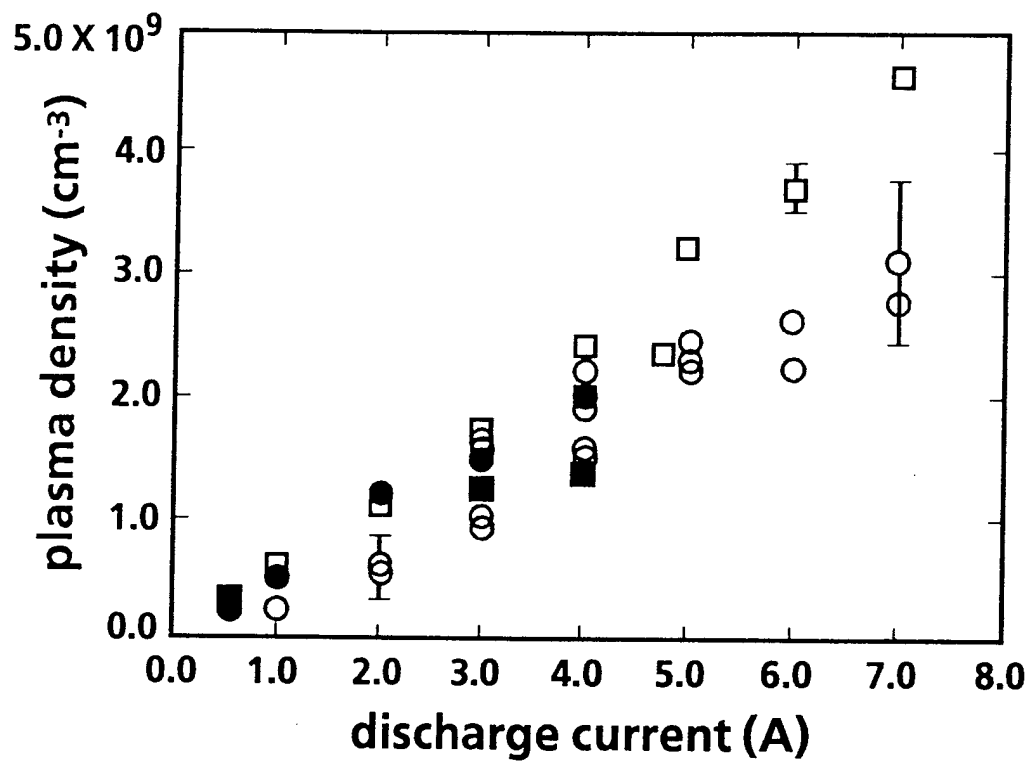


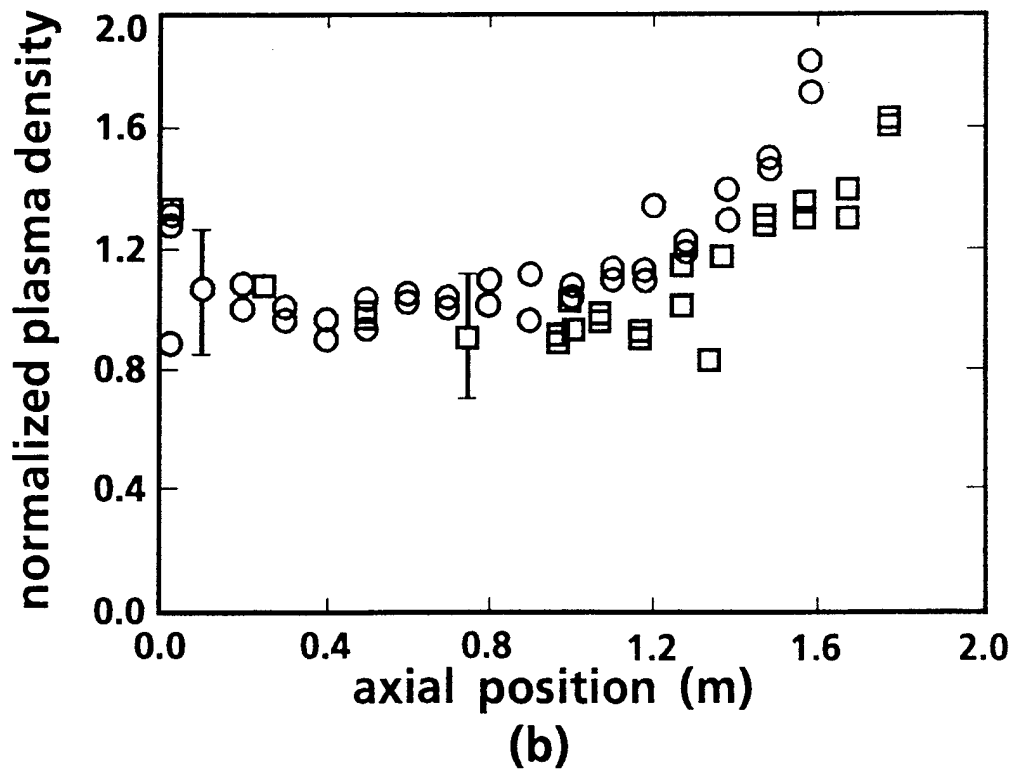
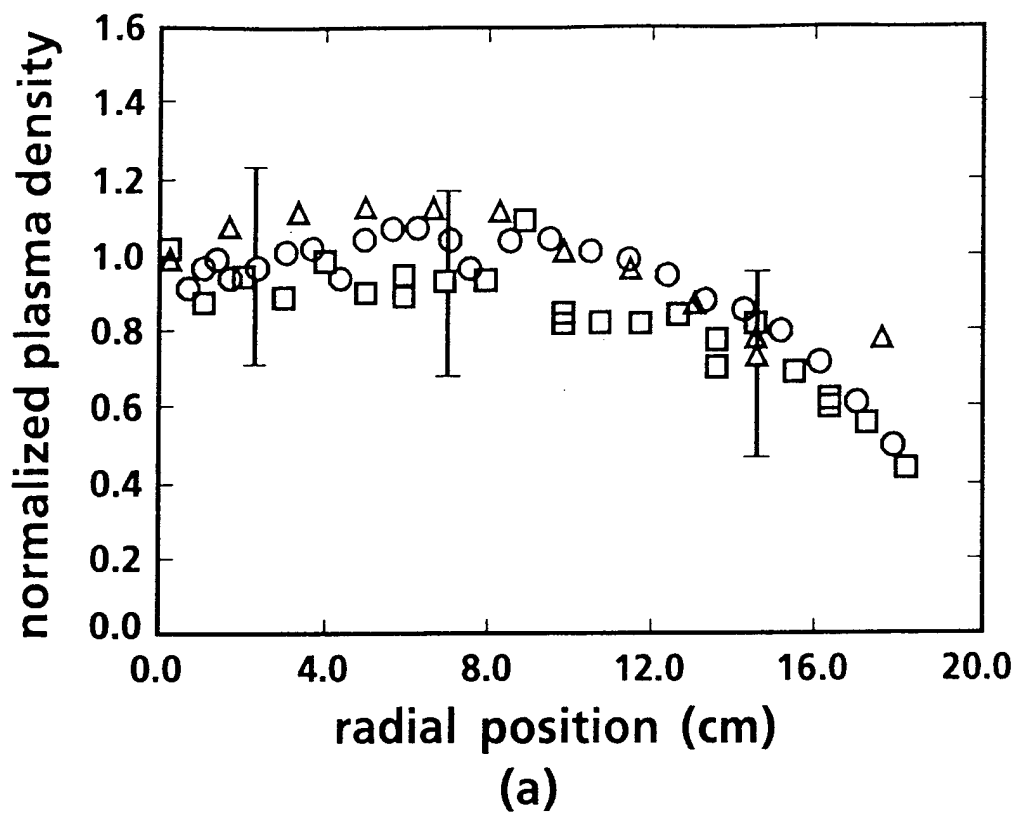


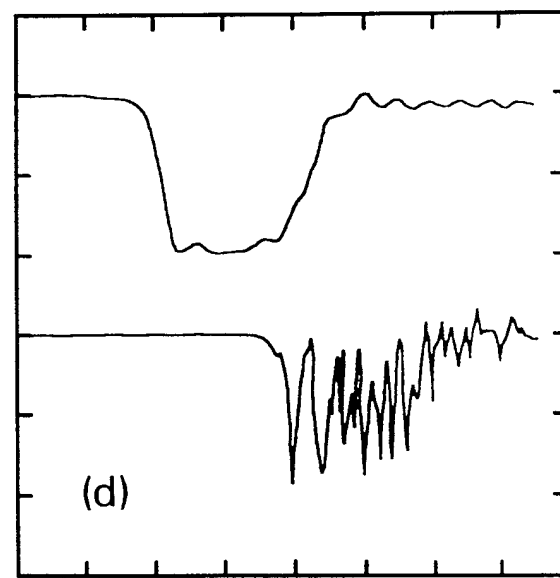
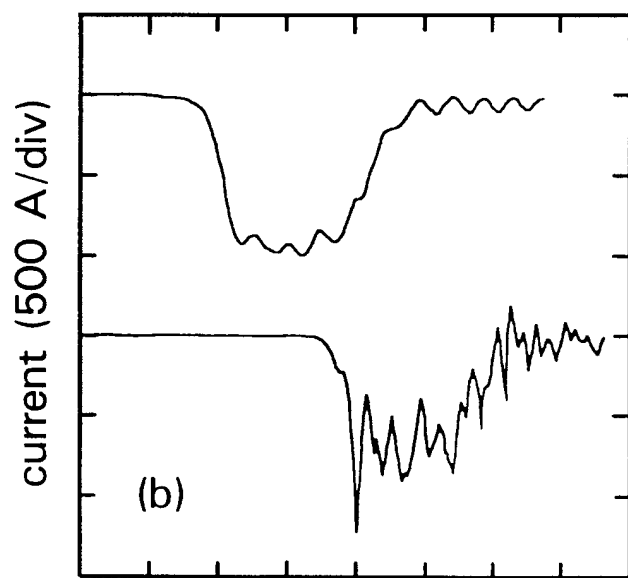
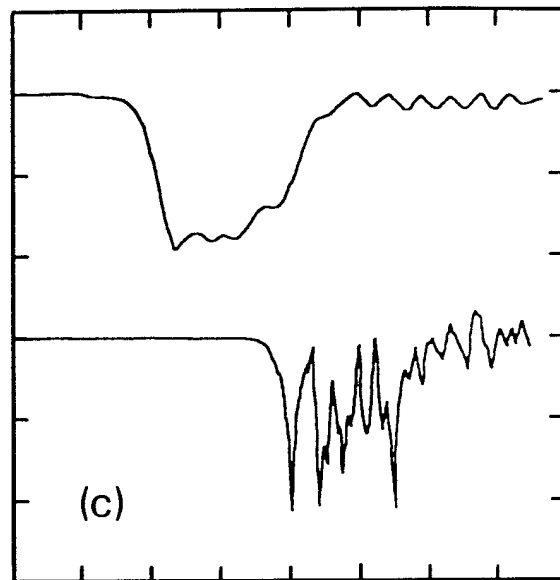
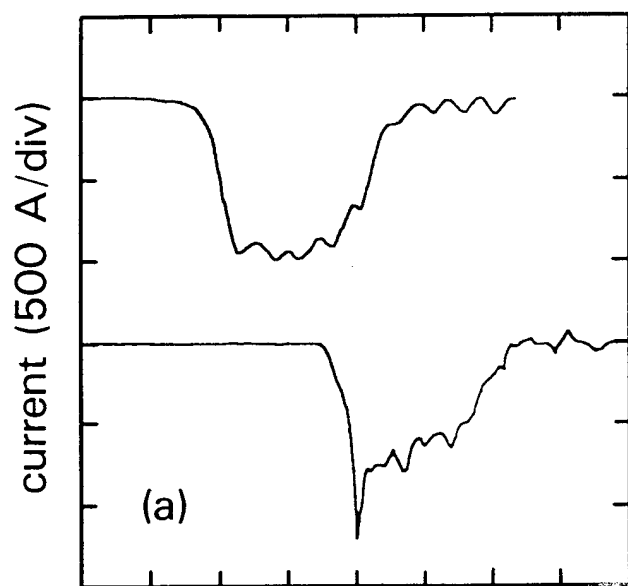








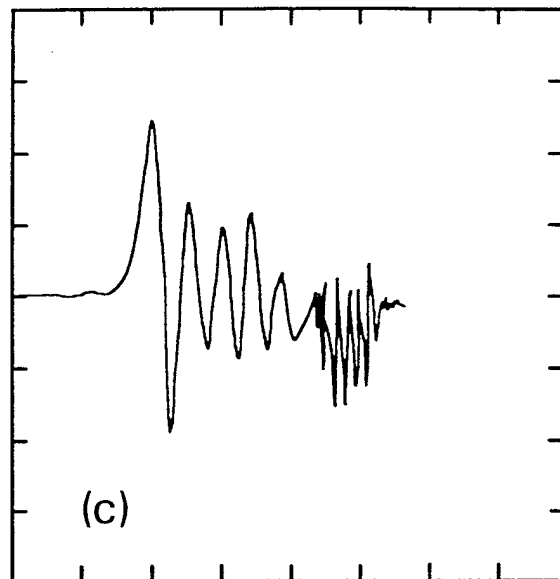
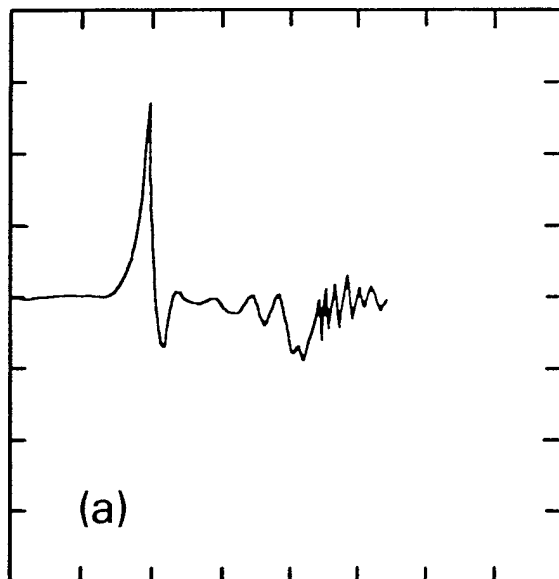




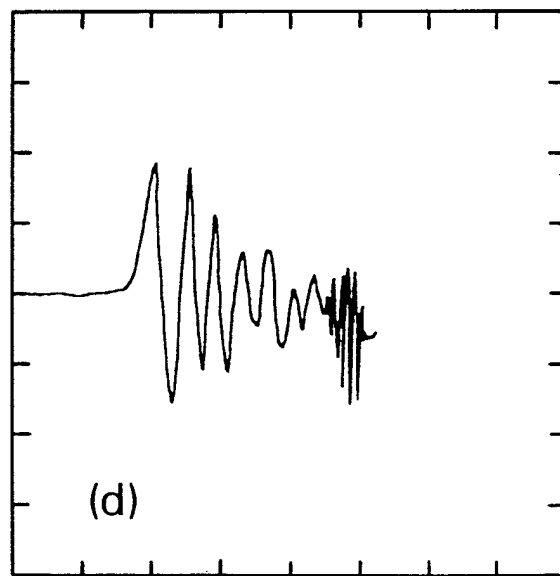
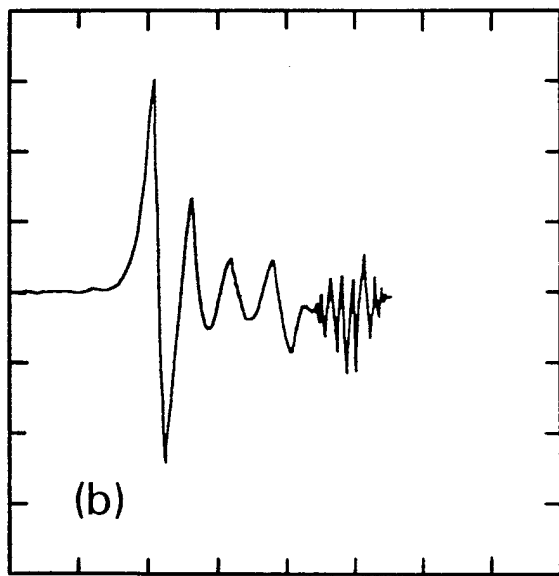
10 ns/div

10 ns/div

unintegrated B-dot signal
(0.5 V/div)



unintegrated B-dot signal
(0.5 V/div)



10 ns/div

10 ns/div

